Determining the resolution limits of electron-beam lithography: direct measurement of the point-spread function

Vitor R. Manfrinato[a], Jianguo Wen[b], Lihua Zhang[c], Yujia Yang[a], Richard G. Hobbs[a], Bowen Baker[a], Dong Su[c], Dmitri Zakharov[c], Nestor J. Zaluzec[b], Dean J. Miller[b], Eric A. Stach[c], and Karl K. Berggren[a,*].

[a] Electrical Engineering and Computer Science Department, MIT

[b] Electron Microscopy Center, Argonne National Laboratory

[c] Center for Functional Nanomaterials, Brookhaven National Laboratory

* Corresponding author: berggren@mit.edu

Table of Contents

1. Spherical- and chromatic-aberration corrected energy-filtered TEM
2. Assumptions and calculation of the direct-beam point-spread function
3. Electron energy loss spectroscopy
4. Volume-plasmon PSF: Kramers-Krönig Analysis
5. Atomistic Simulation of HSQ Interband Transitions
6. Simulation of the secondary-electron point-spread function
7. Monte Carlo simulation of the lithographic point-spread function
    7.1. Stopping power
    7.2. Elastic cross section
    7.3. Inelastic cross section
8. Lithographic point-spread function
    8.1. Sample processing
    8.2. STEM lithography
    8.3. TEM metrology
    8.4. Lithographic point-spread function: dot-exposure method
9. Lithographic point-spread function and its components
10. References

1. Spherical- and chromatic-aberration corrected energy-filtered TEM

We performed energy-filtered transmission electron microscopy (EFTEM) on the sample described in Figure 2a (main text), consisting of a 20-nm-thick HSQ film on top of a 10-nm-thick SiN_x membrane.

EFTEM analysis operating at 200 keV with a FEI-TITAN, equipped with CEOS spherical- and chromatic-aberration correction (ACAT) was completed at Argonne National Laboratory. The chromatic aberration coefficient was 1 μm and the spherical aberration coefficient was 2.5 μm. We used a 50 μm diameter condenser aperture and focused the electron beam to a 0.8 nm FWHM spot, with a beam current of 230 pA. The sample was determined to be in focus by observing the phase-contrast and the Fast Fourier Transform of the image. In order to measure the electron-beam energy loss and maintain the incoming beam energy at 200 keV (as done in conventional electron-beam lithography (EBL)), we used the drift tube energy shift to set the spectrometer to a given energy and used a 5 eV energy slit for energy filtering. Due to the use of the drift tube, we considered data with energy loss less than 120 eV. Energy losses of more than 200 eV from the drift tube may affect the alignment of electron-optics. The spectrometer collection aperture used was 2 mm in diameter. We used a chromatic-aberration-corrected EFTEM to avoid chromatic aberrations in the objective lens. Therefore, the change of the transmitted electron spatial distribution as a function of energy loss was due to scattering in the sample, not due to the inability of the objective lens to properly focus these electrons on the conjugate image plane. The focal length of the incoming electron beam was not changed during the experiment, again to maintain the standard condition of EBL. The dwell time for image acquisition was varied from 0.1 to 1s to maximize the signal-to-noise ratio. The final EFTEM images were obtained by integrating over 40 frames and were aligned to each other using the built-in beam-drift alignment from Digital Micrograph (Gatan, Inc).

We imaged the transmitted electrons with EFTEM, i.e. the spatial distribution of electrons as a function of energy-loss. The measured transmitted electrons lost energy in the range from zero to 120 eV (±2.5 eV). Figure S1 shows the raw images of transmitted electrons as a function of energy-loss. Each image was taken in a nearby and fresh location of the sample. We observed negligible broadening of the electron-beam for energy-loss less than 90 eV. However, at 95 eV or higher energy-loss, a broader electron-beam was observed due to excitation of Si-L2,3 edges (core electrons).

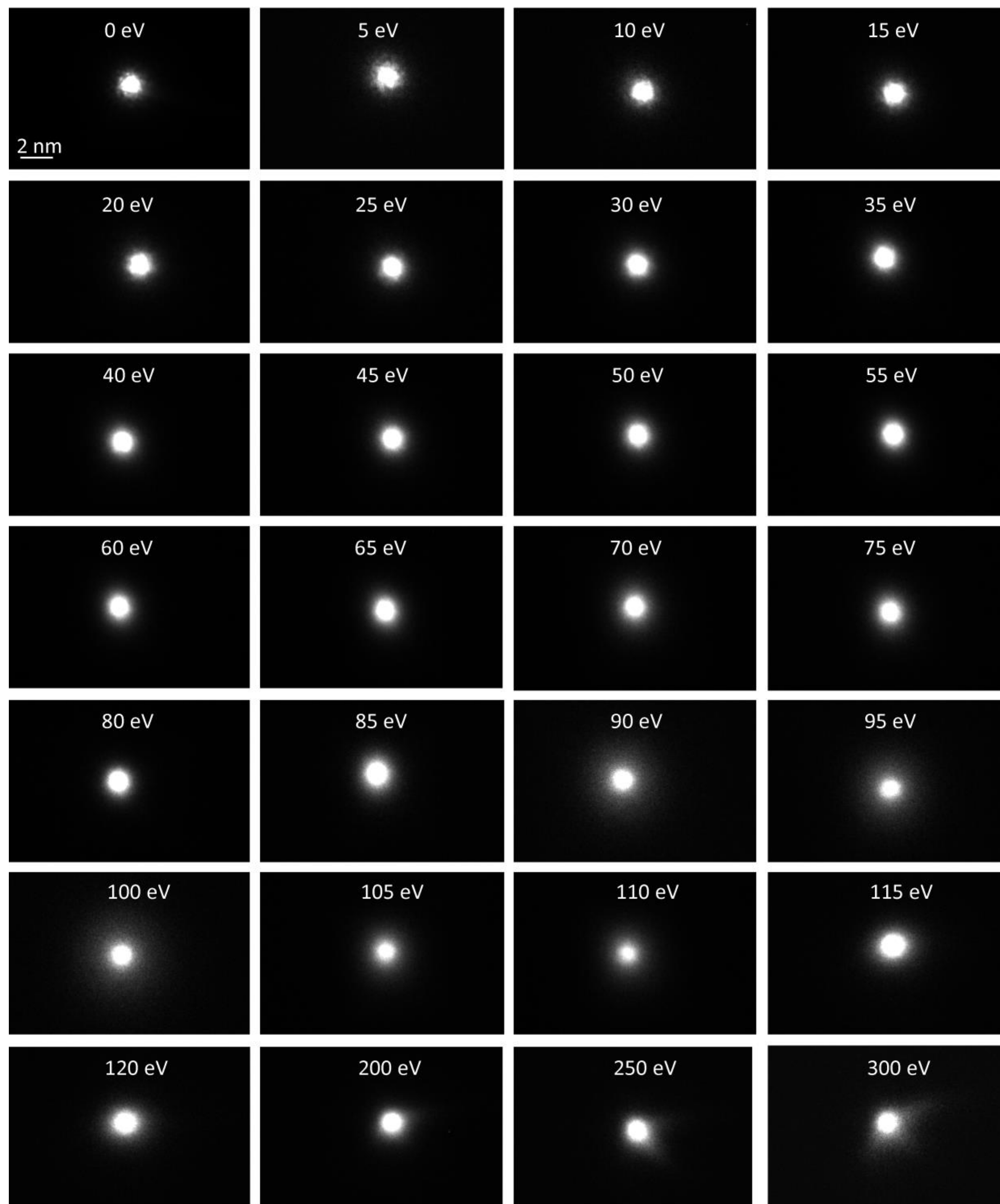

Figure S1. Energy-filtered images of transmitted electrons at 200 keV. The energy-loss ranges from 0 to 300 eV, with a 5 eV width. The dwell time was set to maximize the signal at each micrograph. The sample consists of 20-nm-thick HSQ on top of 10-nm-thick SiN_x. We observe a small spatial broadening of the transmitted electron distribution at

100 eV. For energies higher than 200 eV, we observe an asymmetric electron distribution, possibly due to high energy shift in the spectrometer.

To verify the physical integrity of the sample throughout the EFTEM measurements, we acquired EELS spectra as a function of time. If the electron beam induced sputtering of the sample, we would observe an attenuation of the volume plasmon (VP) peak with respect to the zero loss peak. Figure 2 shows that there was no significant variation in the VP peak intensity for up to 2.5 min of exposure, which is less than the dwell time used for each EFTEM image. We note that each EFTEM image was taken in a nearby and fresh location of the sample. We can observe a minimal decrease in the plasmon peak for exposures longer than 5 min. Consequently, electron-beam induced sputtering is not a critical issue for the image acquisition times used in this experiment.

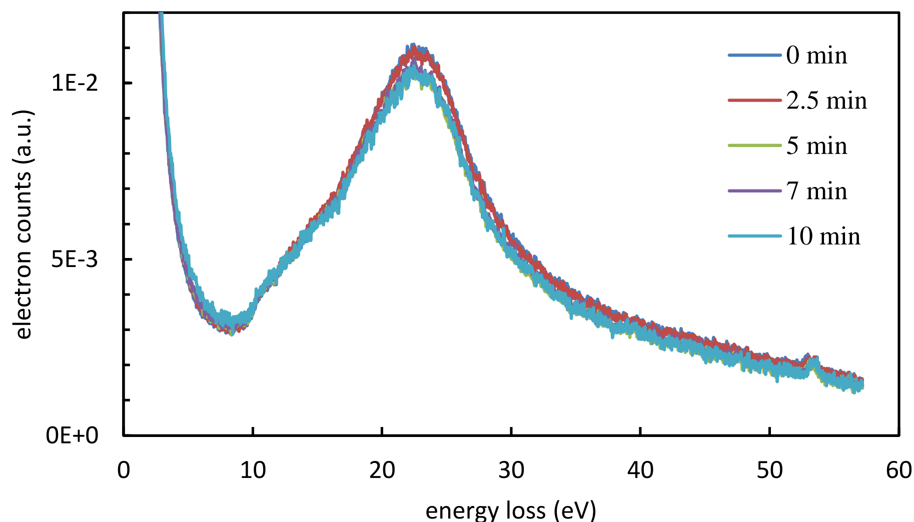

Figure S2. Low-loss electron energy-loss spectra for the HSQ/SiN_x sample at different acquisition times, using a 0.8 nm FWHM spot size at 200 keV. For acquisitions longer than or equal to 5 min we observe a small decrease of the VP peak at 22.5 eV. This indicates minimal electron sputtering of the material.

2. Assumptions and calculation of the direct-beam point-spread function (PSF)

We have two main assumptions for measuring the direct-beam PSF:

(1) We consider that all energy lost by the direct-beam between 5 and 120 eV contributes to resist exposure.

(2) The position of the detected electron beam is approximately the position of the energy lost in the resist. For this consideration, we achieved single scattering regime and calculated that the delocalization of inelastic scattering is not significant compared to the direct-beam PSF.

To verify the appropriate range of energy loss to be taken into account in the direct-beam PSF measurement, we aquired an EELS spectrum from 0 to 700 eV on 20nm/10nm HSQ/SiN_x. We extrapolated the spectrum with a fitting curve up to 1 keV, as shown below. We considered 1 keV as a threshold energy because single inelastic scattering events with energies higher than 1 keV are likely to come from inner-shell ionization and generation of high-energy secondary electrons (SEs), which should not contribute significantly to the sub-10-nm direct-beam PSF. SEs with energies higher than 1 keV will not contribute significantly to the PSF at sub-10-nm radius because these SEs propagate hundreds of nanometers away from the point exposure, creating a uniform background of deposited energy at sub-10-nm radius.

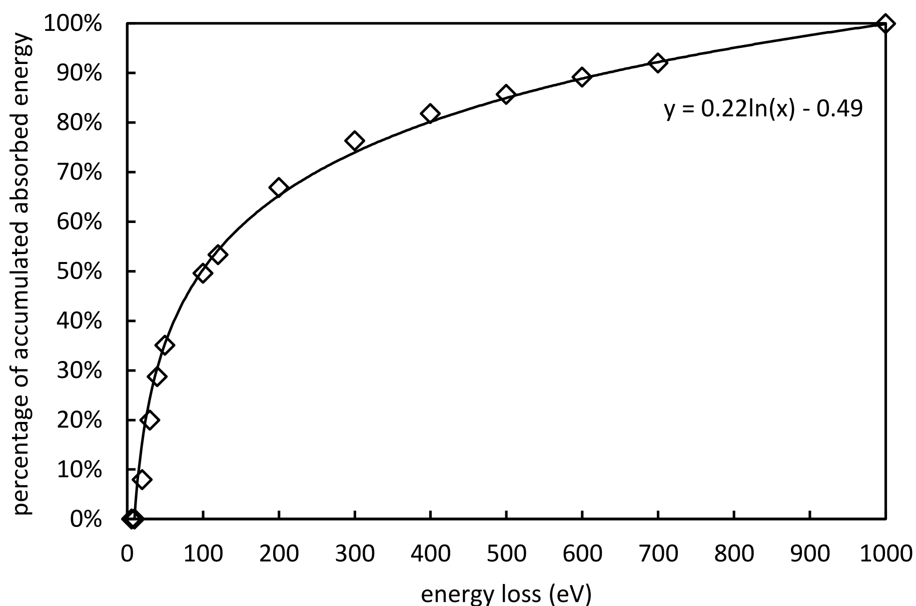

Figure S3. Plot of percentage of accumulted absorbed energy vs energy-loss in the range 10 to a given energy loss . We consider an energy threshold of 1 keV (which is equivalent to 100 %). 53% of the acumulated energy lost was in the 10 to 120 eV range. Single inelastic scattering events with energies higher than 1 keV are most likely to come from inner-shell ionization and generation of high-energy SEs, which should not contribute significantly to the sub-10-nm direct-beam PSF.

If we consider that all energy lost to the sample is due to electrons that lose 10 eV to 1 keV of energy, the 10 to 120 eV energy-loss range contains 53% of total absorbed energy. Therefore, the energy range from 10 to 120 eV captures the majority of the energy-loss of interest. In addition, VP resonance occurs between 10 and 50 eV, which contains 35% of the total absorbed energy. However, we note that the integrated tail of the VP peak extends up to ~100 eV. For example, a portion of the energy loss at 100 eV may be due to VP excitation.

Furthermore, we measured the energy-density threshold for HSQ exposure. We measured an average energy-loss per electron of 4.2 eV for a sample consisting of 20-nm-thick HSQ on top of 10-nm-thick SiN_x. We have estimated that HSQ absorbs 62% of the total energy-loss, and we

considered a threshold dose for large area exposure of 230 electrons/nm^2. Therefore, we have estimated that the threshold energy density for HSQ exposure is ~30 eV/nm^3.

To evaluate our hypothesis of a single scattering regime in our HSQ+SiN$_x$ sample, we measured the log-ratio relation[1]:

$$\frac{t}{\lambda} = \log \frac{I_{total}}{I_{zero}} \quad (1)$$

where t is the sample thickness (HSQ+SiN$_x$), λ is the inelastic mean free path, I_{total} is the integrated EELS or summed EFTEM over all the spectrum, and I_{zero} is the integrated zero-loss peak of the EELS or the EFTEM zero loss peak. Single scattering regime requires $t/\lambda < 1$.The t/λ measured was 0.26 using EFTEM and 0.24 using EELS (and 0.12 for SiN$_x$ only). Therefore, we may assume that the sample was in the single-scattering-event regime.

To evaluate whether inelastic scattering delocalization is critical to our analysis, we calculated the delocalization PSF based on an analytical formulation previously reported.[2] Figure S4 shows that the delocalization PSF decays by more than 4 orders of magnitude from 0.1 to 12 nm radius. The direct-beam PSF does not account for delocalization, but such effects would introduce a negligible broadening to the direct-beam PSF. Delocalization of inelastic scattering for energy loss larger than 25 eV is also negligible compared to the secondary-electron (as previously reported in electron-beam-induced deposition[3]) and volume-plasmon PSFs.

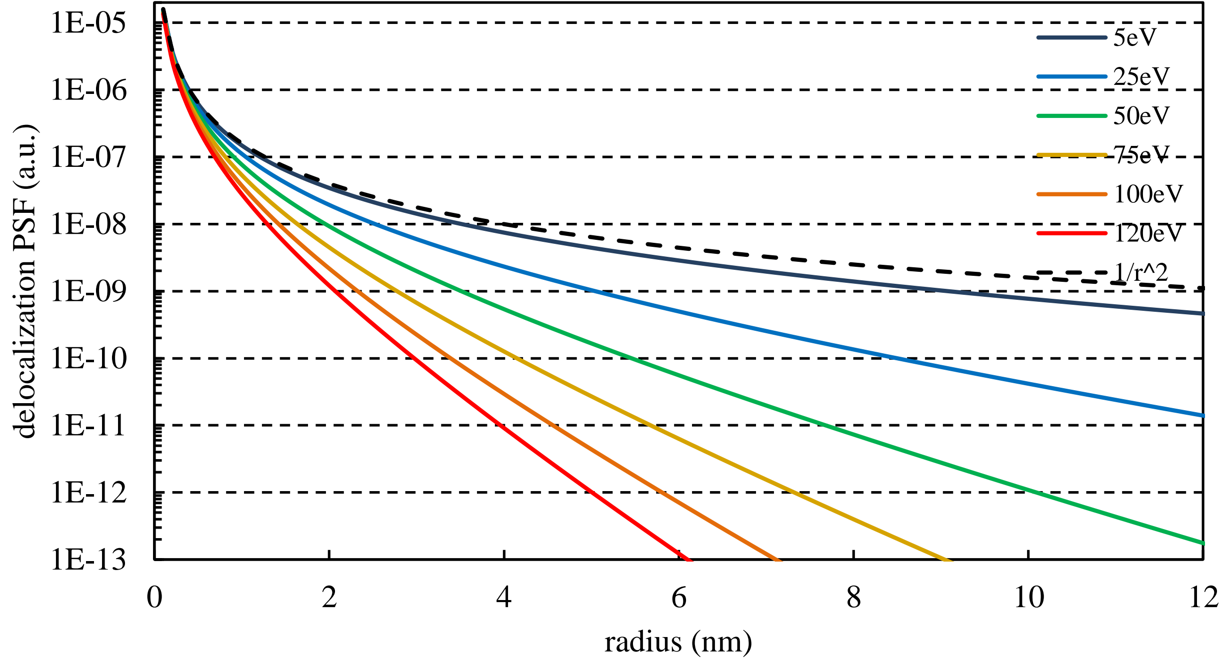

Figure S4. Radial distribution of the probability of energy loss (for 5, 25, 50, 75, 100, and 120 eV), that is, the inelastic or delocalization PSF.[2] The incident electron energy was 200 keV.

We have calculated the energy deposited by the electron beam, called 'direct-beam PSF', by weight averaging of the intensity of transmitted electrons from 2.5 to 122.5eV energy-loss (shown in Figure 2d and Figure 4b of the main text):

$$PSF_{(r)}^{direct-beam} = \sum_{\varepsilon_f=5eV}^{120\ eV} \varepsilon_f \rho_{EFTEM}(r;\ \varepsilon_f) \tag{2}$$

where ε_f is the filtered electron energy loss (using a 5 eV slit), $\rho_{EFTEM}(r;\ \varepsilon_f)$ is the electron counts per second as a function of radial distance r at a given energy loss ε_f.

3. EELS

Electron energy-loss spectroscopy (EELS) was performed on a Hitachi 2700C dedicated aberration-corrected STEM with a cold-field-emitter source (~ 0.4 eV energy spread) at 200 keV. A beam current of ~20 pA, 0.05 - 0.3eV/channel dispersion (depending on the desired energy

range) and 2 mm collection aperture were used. The electron beam convergence semi-angle was 28 mrad, and the collection semi-angle was 14 mrad. The spectrum was taken with 0.04s dwell time with 10-50 frames.

The angle/momentum-resolved EELS was done on a FEI Tecnai F20ST TEM/STEM with a field-emitter-source (~1eV energy spread). An acceleration voltage of 200 kV, beam current of 60 pA, illuminated area 1.3 µm in diameter, 0.6 mm collection aperture, 970 mm camera focal length, 0.2eV/channel dispersion, were used. The dwell-time (0.1 to 100 s) and number of frames (1-100) were adjusted to maximize the signal-to-noise ratio without saturating the detector.

The relationship between the angle of an inelastic-scattered electron and the transferred momentum is[2]:

$$q^2 \cong {k_0}^2\left(\theta^2 + {\theta_E}^2\right) \tag{3}$$

where k_0 is 2505 nm^{-1} for 200 keV incident electrons, and $\theta_E$is 0.065 mrad for 22.5 eV energy loss also with 200 keV incident electrons.

We calibrated the angular scale with a <111> oriented single-crystal silicon film. In the diffraction plane shown in Figure S5, we first aligned the [000] beam (non-diffracted) with the collection aperture. Then, we calibrated the beam tilt necessary to translate the [220] diffracted beam to the position of the [000] beam. The beam tilt was calibrated using an in-house computer script. Therefore, the tilt from [000] to [220] on Si corresponded to two times the Bragg scattering angle for the <220> direction, e.g. 13 mrad. EELS spectra were recorded only for specific values of scattering angle, from zero to 19.5 mrad with varying angular step size. The electron beam incident outside of the collection aperture was therefore blocked. The angular resolution was given by the collection angle or collection aperture size, corresponding to 0.32 mrad and 0.6 mm respectively. The convergence angle was also set to 0.32 mrad. The calibrated EELS system was then used to measure angle-resolved EELS for SiN_x, and HSQ.

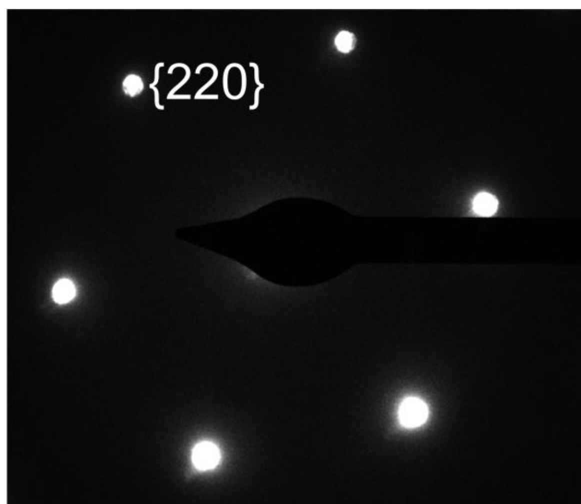

Figure S5. Electron diffraction of single-crystal Si oriented in the <111> direction. The <111> direction is into the plane of the page and is represented by the central spot, which was covered to enhance image-contrast. The six hexagonally arranged spots represent diffraction from the family of crystal planes[4] as shown.

The angle-resolved EELS spectrum of ~25 nm thick HSQ on top of 10-nm-thick SiN_x is shown in Figure S6 below. We observed from Figure S6, and Figure 3 in the main text, that the VP dispersion is subtle, shifting by 1.3 eV for a change in scattering angle of 0.0 to 4.5 mrad.

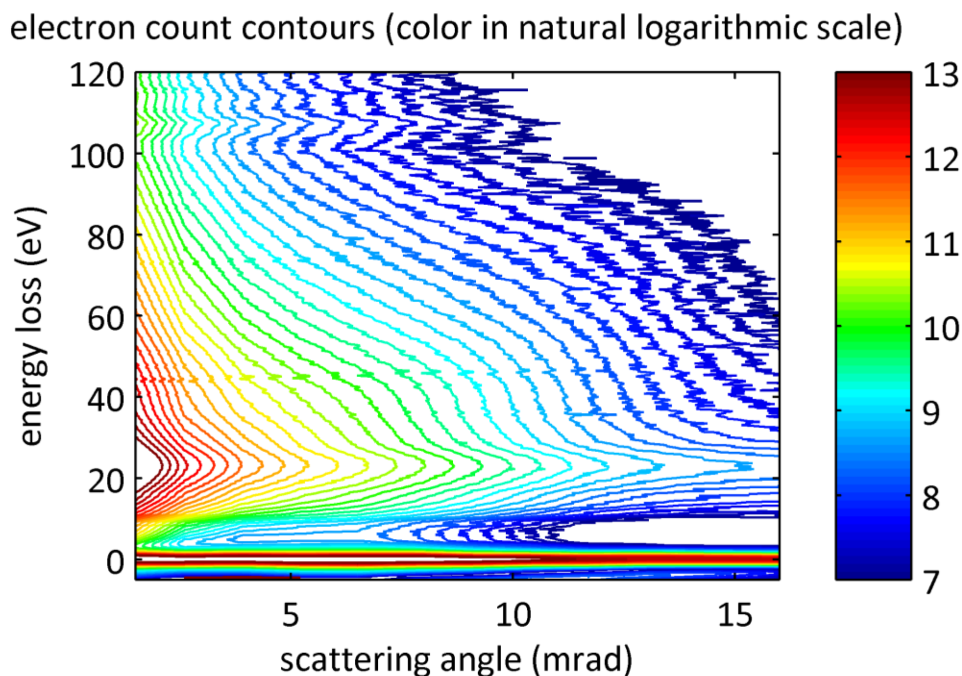

Figure S6. Momentum- or angle-resolved EELS. Electron count contours plotted as a function of electron energy-loss and scattering angle. The electron counts are shown in natural logarithmic scale. We observed the VP peak at 22.5 eV. We also observed a 'shoulder' that increases in intensity with increasing energy and line-width, which we call the dispersive VP component. See Figure 3e in the main text for the VP dispersion in HSQ.

The volume-plasmon peak usually presents a dispersive (leads to shift in energy) and a non-dispersive component. The non-dispersive component is due to a double scattering process, being an elastic scattering event with exchange of momentum plus a VP scattering event without exchange of momentum. In Figure S7 we plotted the ratio of volume-plasmon intensity to the zero-loss intensity. We observed that, above 5 mrad, the VP peak intensity correlated well with the zero-loss peak intensity. This suggests that the energy-loss spectrum above 5 mrad was dominated by the non-dispersive VPs. The observation of the dispersive VP peak in Figure 3e is expected because the maximum angle in Figure 3e is 4.5 mrad.

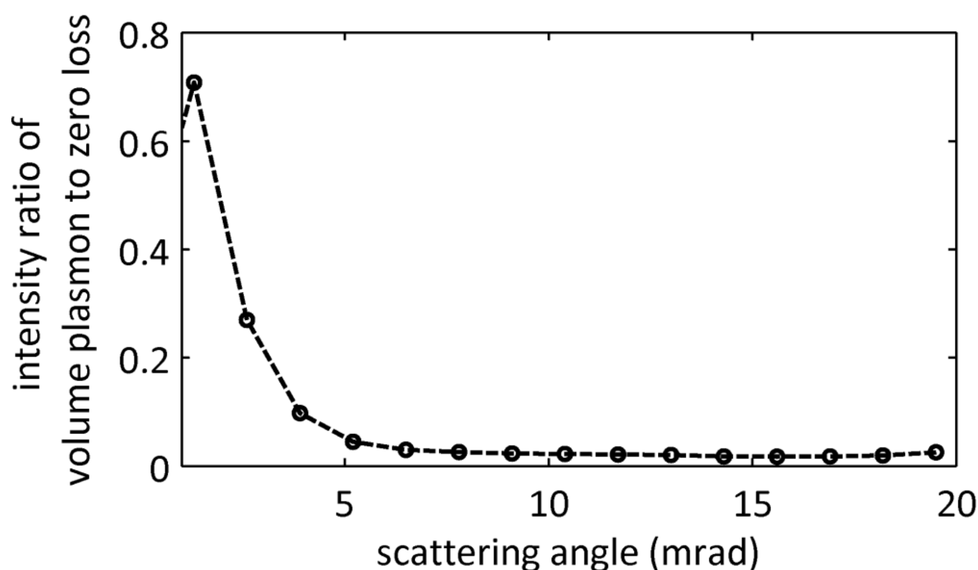

Figure S7. Ratio of the volume-plasmon intensity to the elastic (or zero loss) intensity as a function of scattering angle. We observed that the VP peak intensity correlated well with the elastic peak intensity for scattering angles larger than 5 mrad. This correlation suggests that the energy-loss spectrum is dominated by non-dispersive VPs for scattering angles larger than 5 mrad.

There are two factors to take into account in the EELS spectra shown in Figure 3e-f in the main text and in Figures S6 and S7: (1) the effect of SiN_x membrane; and (2) the effect of electron-beam damage.

We measured the t/λ ratio as discussed in the previous session to quantify the amount of energy-loss in 10-nm-thick SiN_x and ~25-nm-thick HSQ. For these experiments the collection aperture was 3 mm. We would like to perform measurements in a HSQ film that is thick enough to have the majority of the EELS signal from HSQ and not from SiN_x. We would also like to be in the single-scattering-event regime (t/λ <1). The log-ratio for 10-nm-thick SiN_x is $t/\lambda_{SiNx} = 0.18$. While the log-ratio for ~30-nm-thick HSQ on top of 10-nm-thick SiN_x is $t/\lambda_{HSQ+SiNx} = 0.40$. We estimated that 60% of energy-loss from the HSQ/SiN_x sample occurred in HSQ and that both samples were sufficiently thin to remain in the single-scattering-event regime.

To evaluate beam-damage, we noticed that the longest EELS acquisition time was 500 s (60 pA beam current), over a 1.3 µm diameter area, for 30 different scattering angles at the same position in the sample. We imaged the exposed area and monitored the VP peak before and after all acquisitions. We did not observe signs of sample damage (*e.g.* reduction of VP intensity).

4. Volume-Plasmon point-spread function: Kramers-Krönig Analysis (KKA)

The KKA method is discussed in details by Egerton in Reference 2. This method permits calculation of the dielectric function as a function of energy-loss. First we obtain the energy-loss function from the electron energy-loss spectrum in the single scattering regime:

$$J^1_{(E)} \approx S_{(E)} = \frac{I_0 t}{\pi a_0 m_0 v^2} Im\left[\frac{-1}{\varepsilon_{(E)}}\right] ln\left[1 + \left(\frac{\beta}{\theta_E}\right)^2\right] \quad (4)$$

J^1(E) is the electron energy-loss spectrum; S(E) is the electron energy-loss spectrum in the single scattering regime; I_0 is the intensity of the zero loss peak; t is the sample thickness; a_0 is the Bohr

radius; m_0 is the electron rest mass; v is the incident electron velocity; $\mathcal{E}$(E) is the dielectric function; β is the collection semi-angle; θ_E is the characteristic scattering angle; and E is the energy loss.

The energy loss function, $Im\left[\frac{-1}{\varepsilon_{(E)}}\right]$, is related to the dielectric function $\varepsilon_{(E)}$. By using the KKA sum rule and KKA transformation, $\varepsilon_{(E)}$ is obtained. The complex index of refraction is then obtained by:

$$\boldsymbol{n} = n + ik = \sqrt{\boldsymbol{\varepsilon}_{(\boldsymbol{E})}} = \sqrt{\boldsymbol{\varepsilon}_{\boldsymbol{1}(\boldsymbol{E})} + \boldsymbol{i}\boldsymbol{\varepsilon}_{\boldsymbol{2}(\boldsymbol{E})}} \tag{5}$$

We assumed that the VP decay length is the same as the decay length of an electromagnetic wave at the same frequency. A detailed discussion on the validity of this assumption can be found in References [5, 6]. The decay length L is the length scale where the intensity of the VP decays to 1/e of its original value:

$$L = \frac{\lambda_{0(E=22.5\ eV)}}{4\pi k_{(E=22.5\ eV)}} \tag{6}$$

where $\lambda_0$is the VP wavelength in vacuum, and k is the extinction coefficient or imaginary part of the complex index of refraction, both at the VP frequency.

Finally, the VP PSF is calculated using the relation:

$$PSF_{(r)}^{volume-plasmon} = \frac{e^{-r/L}}{2\pi r}\left[\frac{1}{nm^2}\right] \tag{7}$$

The factor $1/r$ is due to the cylindrical symmetry of the VP generation and propagation from a linear source perpendicular to the resist surface (the electron beam). This PSF form is similar to those used previously.[5, 7, 8]

5. Atomistic Simulation of HSQ Interband Transitions

Atomistic simulation of HSQ was performed with the *Abinit*[4, 9] package using projector augmented wave (PAW) density functional theory (DFT) under the local density approximation (LDA). To simulate a single HSQ cage molecule ($H_8Si_8O_{12}$) containing 28 atoms, the molecule was placed in a large vacuum box with dimension of $20 \times 20 \times 20$ $Bohr^3$. Different box sizes were tested and convergence was achieved for the chosen box size. The maximal plane-wave kinetic energy cutoff in the simulation was set to 50 Hartree. Convergence was also confirmed for this parameter value. Since the molecule-in-box model represents an isolated system, only one k point was included in the k-grid for the calculation.

5.1. Geometry Optimization

We first optimized the structure of the HSQ cage using Broyden-Fletcher-Goldfarb-Shanno minimization. The HSQ cage structures before and after optimization are illustrated in Figure S8. Simulated structural parameters are compared to experimental values obtained from XRD[10] in Table S1, confirming that the simulation generates correct HSQ cage structure.

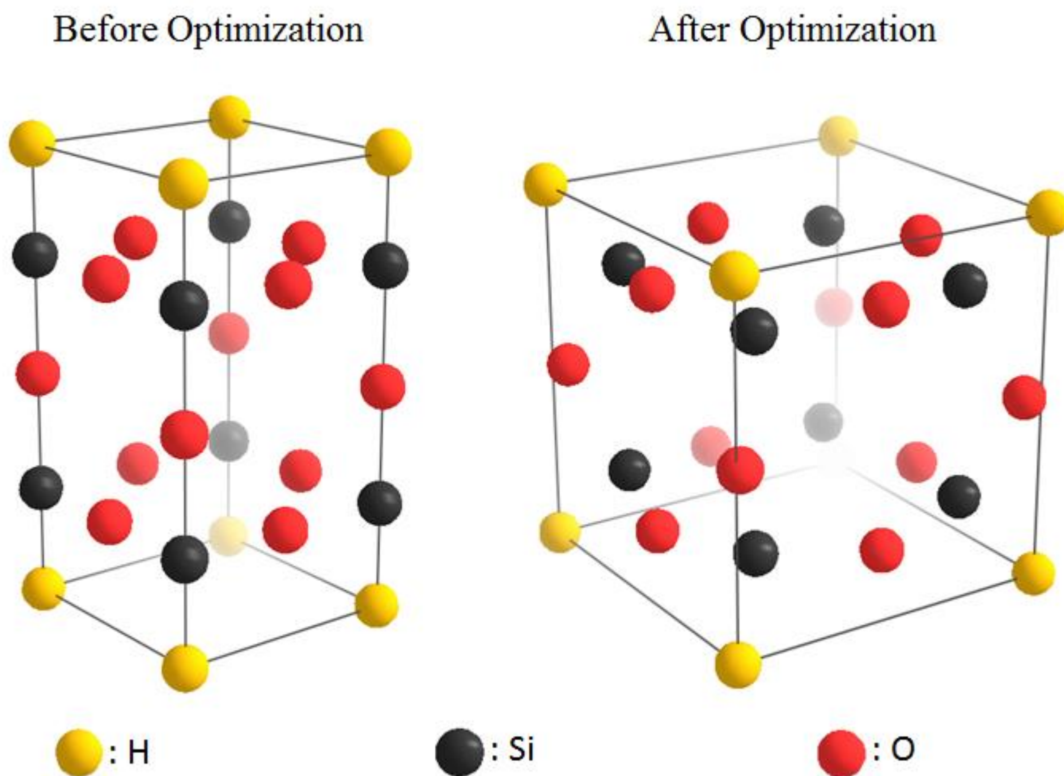

Figure S8. Cage structures of a single molecule of HSQ before and after structural optimization. We note that HSQ is an amorphous material that contains cage and network structures.

	Experiment[10]	Simulation
bond length $R_{Si\text{-}O}$	162 pm	173 pm
bond angle $A_{Si\text{-}O\text{-}Si}$	147.5°	144.5°
bond angle $A_{O\text{-}Si\text{-}O}$	109.6°	108.5°

Table S1. Comparison of structural parameters obtained from experiment[10] and simulation.

5.2. Electronic Structure

We then calculated the electronic structure of a HSQ cage using DFT. Goedecker-Teter-Hutter LDA pseudopotentials[11] were used for H, Si, and O atoms. Only the valence electrons were

considered under the frozen-core approximation. Figure S9 illustrates the calculated density of states (DOS) for a HSQ cage.

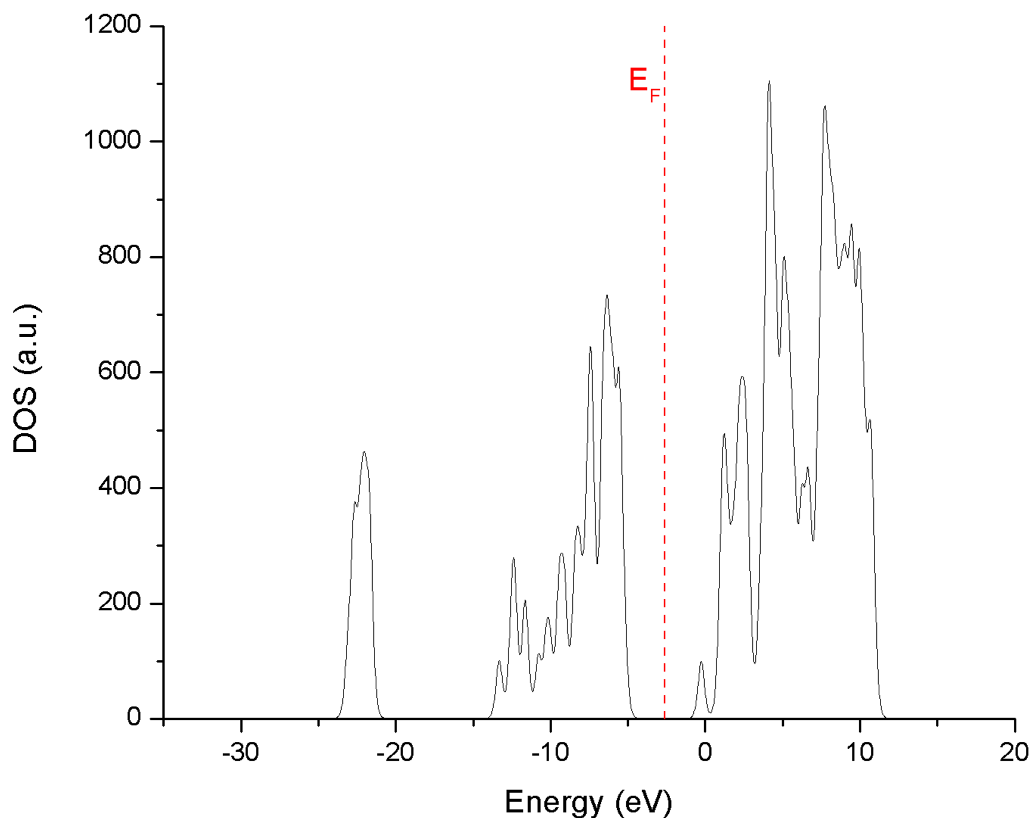

Figure S9. Simulated density-of-states (DOS) for a HSQ cage. The δ function representing each molecular orbital is smeared by an energy of 0.01 Hartree. The Fermi level is indicated by the red dashed line.

5.3. Optical Properties

Simulation of HSQ optical properties is based on the simulation result of its electronic structure. Random phase approximation (RPA) was used to calculate the dielectric function ϵ of HSQ. The energy-loss function was thus calculated from $Im(-1/\epsilon)$. The energy-loss function is shown in Figure S10. By comparing the simulated energy-loss function with experimentally obtained EELS

data, we conclude that the VP resonance is either not resolved or strongly underestimated by the simple DFT-LDA calculation of an isolated HSQ cage molecule. However, interband transitions are resolved and lead to peaks in the simulated energy-loss function. In the experiment, the energy-loss is dominated by VP resonance. So, to better compare the simulation with the experiment and determine the contribution from interband transitions, we performed a second-derivative on the EELS spectrum to find the interband transitions. Table 2 shows the comparison between EELS interband transitions with the simulated interband transitions. For proper comparison, we shifted the simulated peaks by +2.46 eV. It can be seen that simulation and experiment achieve a reasonable agreement. It was necessary to shift the simulated peaks because the DFT-LDA method is known to underestimate the band-gap, or energy intervals between molecular orbitals.

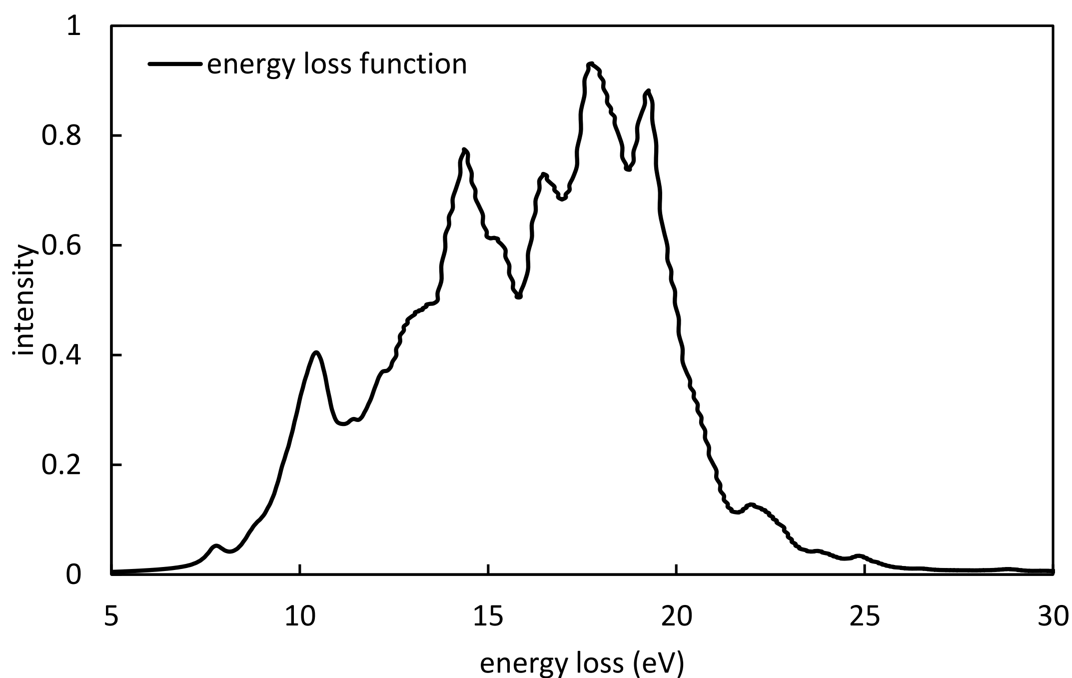

Figure S10. Simulated energy-loss function of an isolated HSQ cage molecule.

measured peaks (eV)	6.3	7	8.5	10.5	12.1	12.9	14.4	-	-	17.3	18.5	19.8	21	22.5
simulated peaks (eV)	-	7.8	-	10.5	12.2	13	14.4	15.1	16.4	17.6	-	19.3	-	22

Table S2. Comparison between measured peaks in the low-loss EELS spectrum with atomistic simulation of interband transitions of HSQ-cage structure.

6. Simulation of the secondary-electron point-spread function

The SE PSF model presented here is inspired by works of Hartley[12] and Neureuther[13] and is illustrated in Figure S11. The model presented here is simplified but effective in giving an intuition of the role of SEs in EBL.

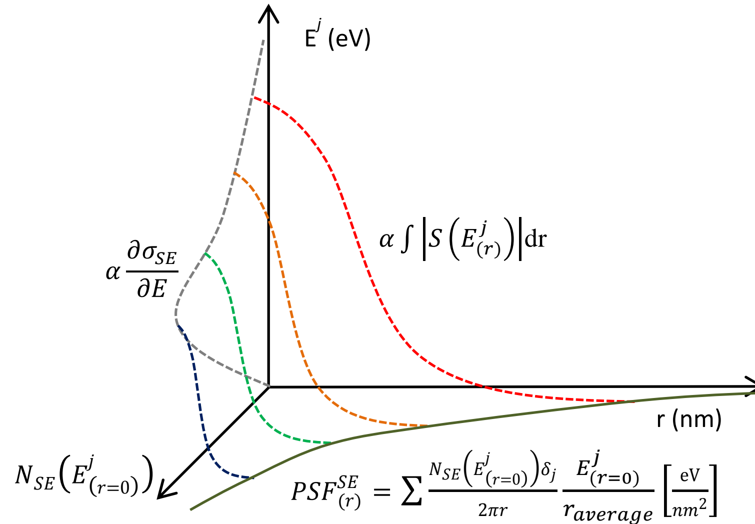

Figure S11. Illustration of the secondary-electron (SE) PSF model. Number of SEs N_{SE} *versus* SE energy E^j *versus* radial distance *r*. The number of SEs as function of energy is given by the differential cross-section $\frac{\partial \sigma_{SE}}{\partial E}$. From the position r=0, the SEs travel away from the center losing energy continuously. The colored lines represent the energy of SEs at different initial energies at *r*=0. High-energy SEs propagate longer distances but are in smaller number. The rate of energy loss is given by the modified Bethe stopping power. To estimate the electron penetration depth from the maximum penetration depth, we use the random-walk approximation $r_{average} = \frac{r_{max}}{\sqrt{N}}$, where N is the number of inelastic collisions. The $PSF^{SE}_{(r)}$.is obtained by the summation of the energy loss density of all electrons at a given radius.

<u>SE Generation:</u> The number of secondary electrons generated at radial distance ' *r=0*' with energy $E^{j}_{(r=0)}$ is given by:

$$N_{SE}\left(E^{j}_{(r=0)}\right) = \frac{\partial\sigma_{SE}}{\partial E} n_E N_{pe} l \left[\frac{\#e^-}{erg}\right] \tag{8}$$

$E^{j}_{(r)}$ is the SE energy as a function of radial distance r, starting with energy j at $r = 0$. $\frac{\partial\sigma_{SE}}{\partial E}$ is the classical differential electron inelastic cross section (probability of SE emission per unit energy) for core and valence electrons, n_E is the electron density, N_{pe} is the number of incident primary electrons, and l is the resist thickness.

<u>SE propagation:</u> The maximum propagation and random-walk (based on spherical cross section) estimation of SE propagation is given by:

$$r_{max} \approx \frac{E^{j}_{(r=0)}}{\left|S\left(E^{j}_{(r=0)}\right)\right|} \tag{9}$$

$$r^{j}_{average} = \frac{r_{max}}{\sqrt{N}} \tag{10}$$

where $\left|S\left(E^{j}_{(r-\Delta r)}\right)\right|$ is the stopping power for low-energy electrons, and N is number of inelastic collisions

<u>SE energy deposition:</u> The linear-density of deposited energy along the averaged (random walk) secondary-electron path is given by:

$$\frac{\Delta E^{j}_{(r)}}{\Delta r_{average}} = \frac{E^{j}_{(r=0)}}{r^{j}_{average}} \left[\frac{erg}{nm}\right] \tag{11}$$

<u>SE point-spread function (SE PSF)</u>: The final calculated SE PSF is given by:

$$PSF^{SE}_{(r)} = \sum_{j=10\ eV}^{Eprimary/2} \frac{N_{SE}\left(E^{j}_{(r=0)}\right)\Delta E_j}{2\pi r} \frac{E^{j}_{(r=0)}}{r^{j}_{average}} \delta_{j>\left|S\left(E^{j}_{(r=0)}\right)\right| r^{j}_{average}} \left[\frac{\mathrm{erg}}{nm^2}\right] \tag{12}$$

The term $\delta_{j>\left|S\left(E^{j}_{(r=0)}\right)\right|r^{j}_{average}}$ (=1 if the inequality is satisfied) removes electrons that will not reach a distance $r^{j}_{average}$ from the sum. The term ΔE_j is the energy increment of the sum (1 eV in the simulation in this work).

7. Monte Carlo simulation of the lithographic point-spread function

Our goal is to have a trustworthy Monte-Carlo model to simulate the lithographic PSF and compare with experimental results. The physics of our Monte Carlo code, mainly based on references 14, 15, is summarized below.

7.1. Stopping power: We used Joy's Bethe-modified stopping power[16], which is accurate with respect to experimental data from 50 eV to 30 keV, and is a reasonable approximation from 10 eV to 30 keV.[17] We used the relativistic Bethe stopping power for electrons with energies higher than 30 keV.

7.2. Elastic cross section: We used the Mott elastic cross-section, which is known to be more accurate than Rutherford at lower energies (<10 keV).[18]

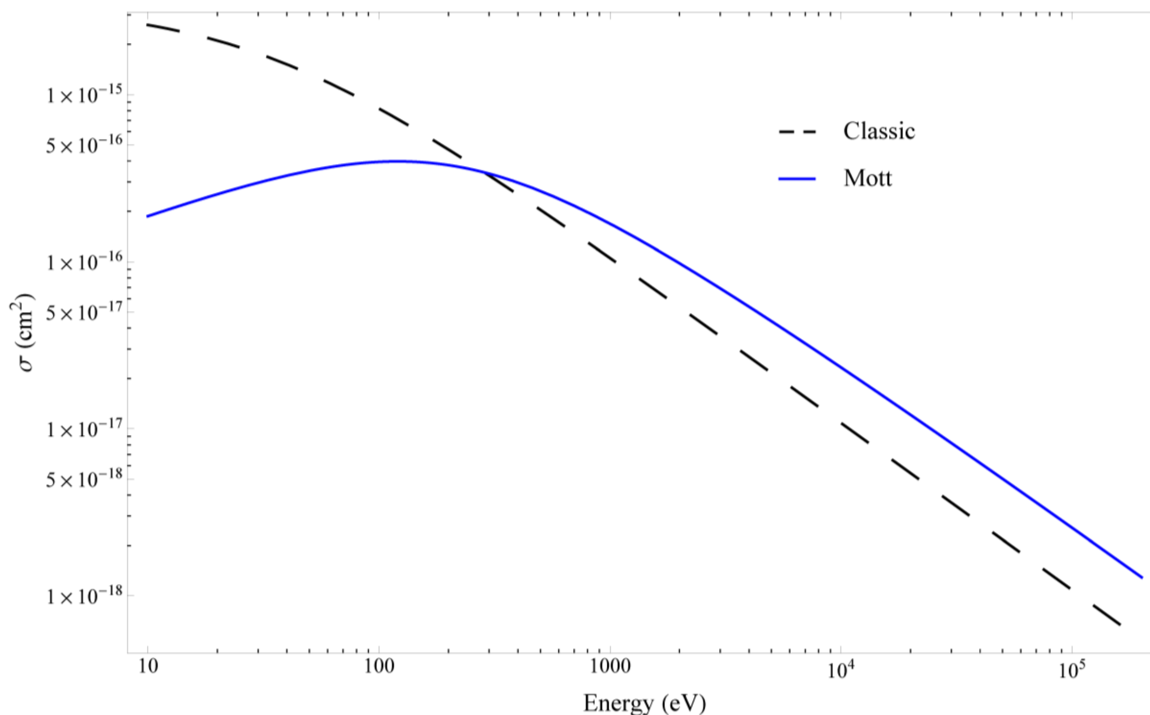

Figure S12. Elastic electron cross-section as a function of incident electron energy. The Mott cross section provides higher accuracy for lower primary electron energies than does the screened Rutherford cross-section.

7.3. Inelastic cross section: In Figure S13 we compared the following inelastic cross sections: (1) Classic;[14](2) Moller (as used in *Casino*[18]); (3) Moller for valence electrons and Gryzinski[19] for core electrons; and (4) Moller for valence electrons and Vriens for core electrons,[12, 13] named "Moller+Vriens". The lower bound cut off energy for inelastic scattered electrons was 10 eV.

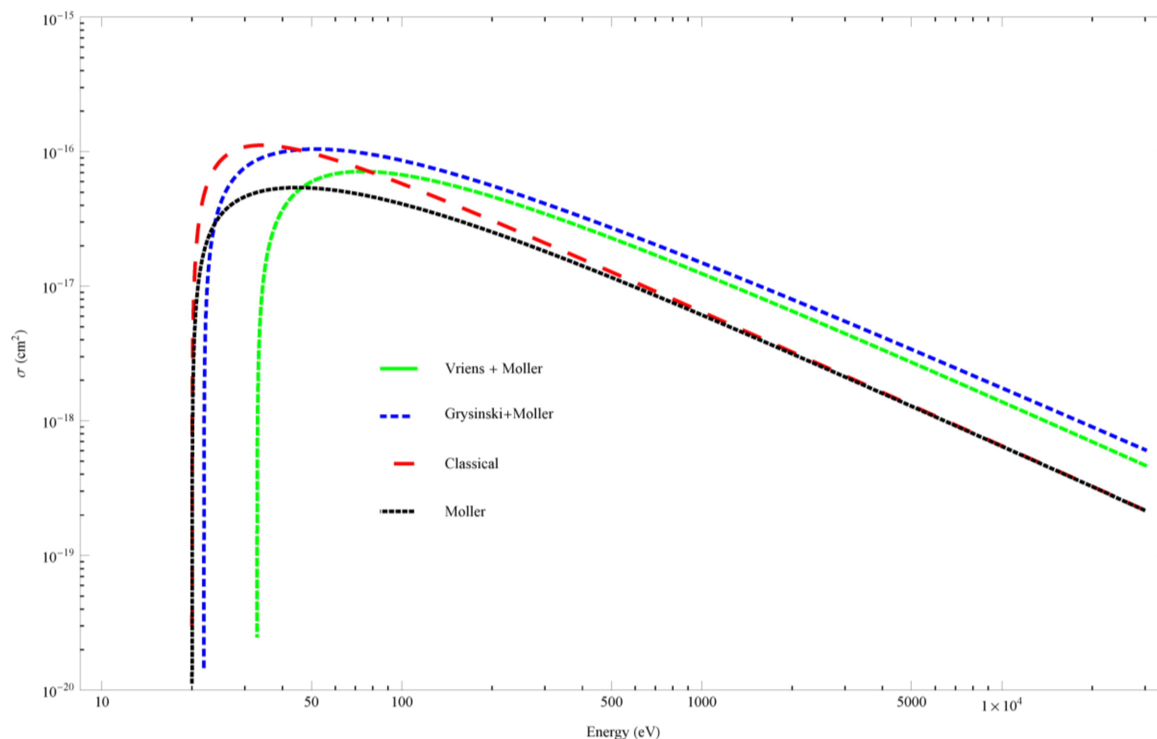

Figure S13. Inelastic electron cross-section as a function of incident electron energy. The Moller model gives the smallest cross-section while Grysinski model gives the largest cross-section for large energies.

We chose to simulate the SEs in the main text using the classical inelastic cross section because this model fits well with the lithographic PSF from ~10 to ~1000 nm.[20-22] We also tested the Moller+Vriens model, which provides a higher inelastic cross-section causing the SEs to have a larger effect on the PSF. As shown in Figure S14, the PSF using the Moller+Vriens model is wider than the PSF with the classic model.

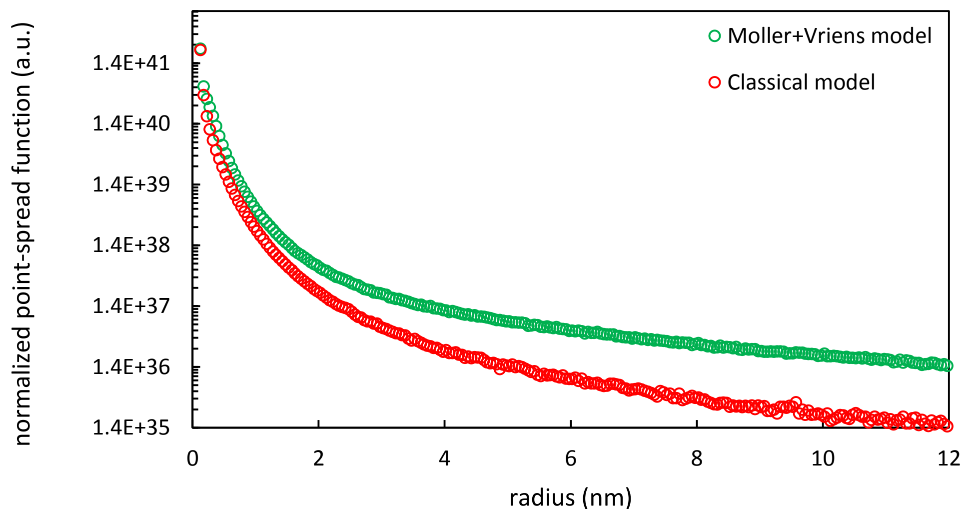

Figure S14. Monte-Carlo-simulated PSFs with different inelastic electron cross-sections. Red circle is the PSF using the classical inelastic cross section, green circle is the PSF with the Moller+Vriens inelastic cross section.

To evaluate whether SEs originated from direct atomic ionization (valence and core electrons) and not VPs (and not SEs generated from VPs) could be responsible for the lithographic PSF, we compared the lithographic PSF to two different Monte-Carlo simulated PSFs. Here, we included the effect of the instrument spot size (shown in Figure 2 of the main text). Figure S15 shows that the classical and the Moller+Vriens inelastic scattering models did not generate PSFs that match the shape of the lithographic PSF. This result suggests that SEs are not sufficient to simulate the lithographic PSF at the sub-12-nm scale. As is discussed in the main text and detailed in the next section, the total deposited energy density including SEs and VPs shown in Figure 4c better represents the lithographic PSF.

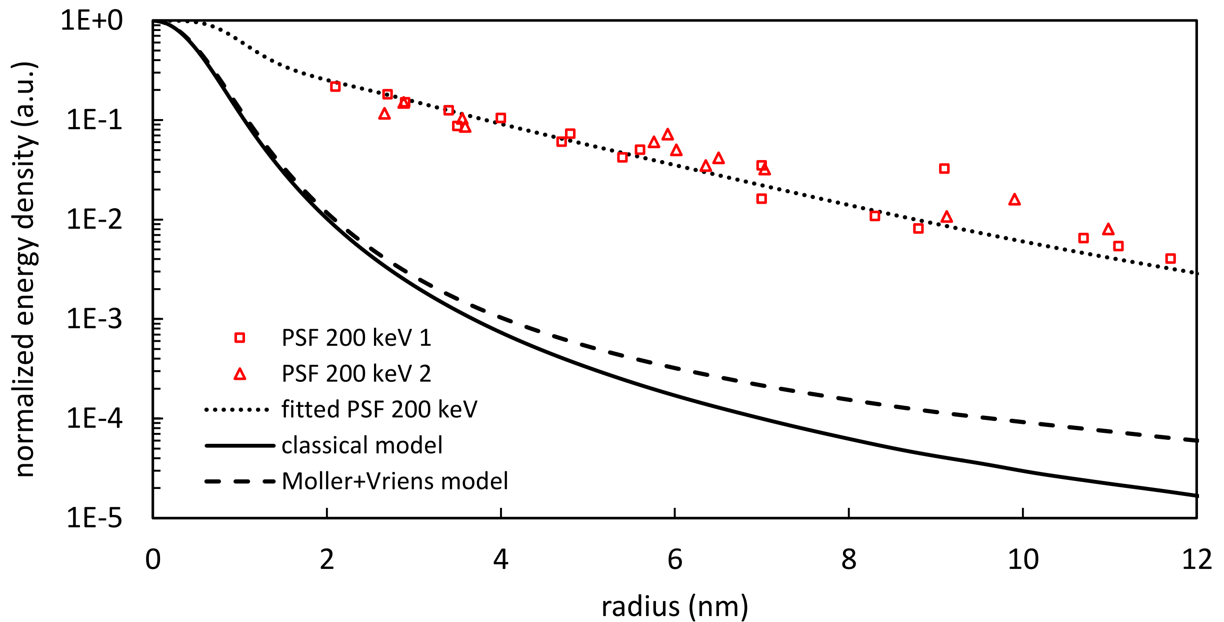

Figure S15. Comparison between the lithographic PSF and Monte-Carlo simulated PSFs convolved with the instrument spot size (maximum value of all PSFs was set to unity): (red squares represent dataset 1 and red triangles represent dataset 2) lithographic PSF from dot-exposure method; (dotted line) fitted lithographic PSF previously reported,[23] which is accurate down to 1 nm radius because this fitted PSF was obtained using 2-nm-wide feature as test structure; (continuum line) Monte-Carlo simulated PSF including SE generation using the classical inelastic cross section model; (dashed line) Monte-Carlo simulated PSF including SE generation using the 'Moller+Vriens' inelastic cross section model. We used the elastic cross section and stopping power models described in section 7.1 and 7.2.

In addition, we compared the Monte Carlo PSF with the numerical SE PSF (both simulations do not include VPs). Figure 4b in the main text shows a significant disagreement between these two models. Figure S16 below shows only a similar trend between these two PSFs from 10 to 100 nm radius. The numerical SE PSF is simplified and it does not take into account the complex scattering by the direct-beam and SEs. Therefore, we rely on the Monte Carlo simulation for analyzing the role of SEs in the lithographic PSF.

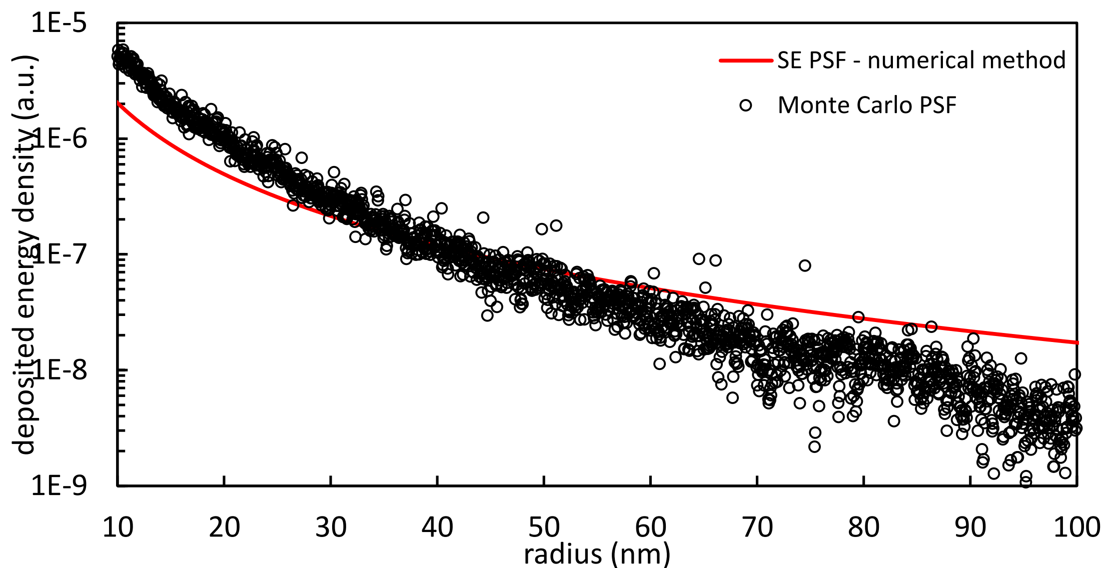

Figure S16. Comparison between the numerical SE PSF, described in the previous section, to the Monte-Carlo PSF. Both PSFs were calculated using the classical inelastic scattering cross section and the modified Bethe stopping power for electron energies smaller than 30 keV.

To understand the effect of backscattered electrons in the PSF, we simulated two PSFs, one with the 10-nm-thick SiN_x supporting membrane (which should not show the effect of backscattered electrons) used throughout this work, and a more traditional 300-µm-thick Si substrate. As shown in Figure S17, the effect of backscattered electrons is apparent for radius larger than 50 nm. Therefore, the PSF measurements presented in the main text are valid for sub-50-nm radius, which can be useful to estimate the resolution limit of dense structures with sub-$50\times50nm^2$ area.

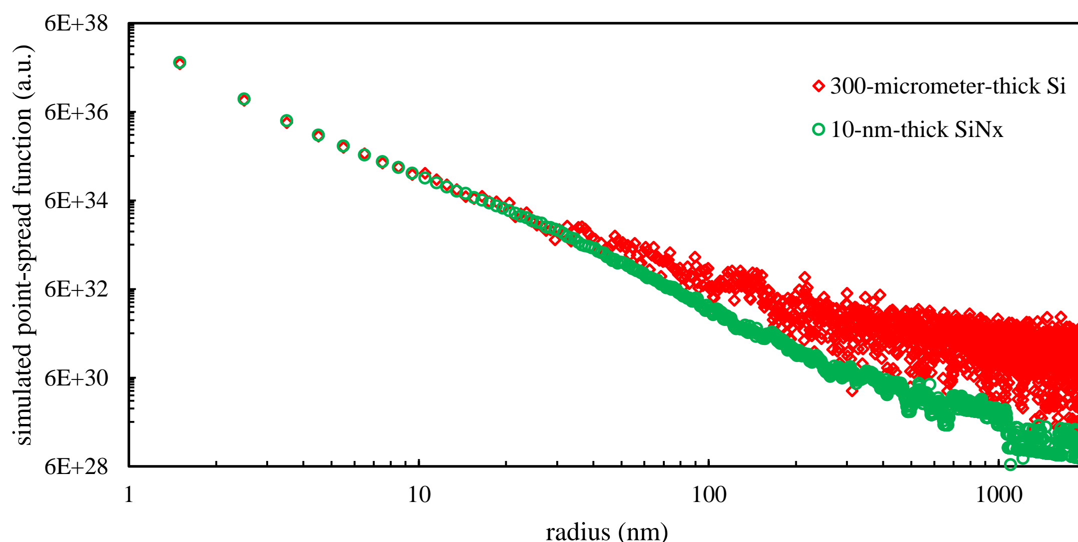

Figure S17. Monte-Carlo simulated PSFs with different supporting substrates. These simulations include SE generation but do not include VP generation. (green circle) Monte-Carlo PSF of 20-nm-thick HSQ on top of 10-nm-thick SiN_x membrane. (red diamond) Monte-Carlo PSF of 20-nm-thick HSQ on top of 300-µm-thick Si substrate. We used the classical inelastic scattering model for both PSFs. The other models used were previously described in this section. We observed a deviation between the PSFs for radius larger than 50 nm.

8. Lithographic point-spread function

8.1. Sample processing

Samples were prepared by spin-coating HSQ (1% solids XR-1541, Dow Corning) on 10-nm-thick SiN_x membranes (TEMwindows.com) at a spin-speed of 8 krpm. The resulting HSQ thickness was 10 nm. To avoid thermally-induced cross-linking of HSQ, which might lead to a loss in resolution, no pre-exposure bake was performed[24]. After exposure, samples were immersed in a salty developer (1% weight NaOH + 4% weight NaCl)[24] for 4 min at 24°C, rinsed under deionized water for 2 min, rinsed in isopropyl alcohol for 10 s, and gently blown dry with nitrogen gas for 1 minute. The typical total processing period from spin coating to development was about 4-5 days.

8.2. STEM lithography

Exposures were performed on a Hitachi HD 2700C dedicated aberration-corrected scanning transmission electron microscope (STEM) with a cold-field-emitter source (~ 0.4 eV energy spread), 0.15 nm spot size[25], and a beam current of 70-100 pA.

We did our exposures by imaging the resist with a Digiscan Control Unit, embedded within the Digital Micrograph Suite (Gatan, Inc.) choosing: (1) the desired dwell time; (2) microscope magnification; (3) number of pixels; and (4) beam current. These parameters define the area and pitch of interest. No pattern generator was used.

8.3. TEM metrology

The TEM metrology was done on a JEOL JEM 2010F transmission electron microscope at 200 keV. A standard <011> Si sample was used to calibrate the magnification for the TEM camera. The images were taken slightly defocused in order to provide a slight Fresnel fringe to enhance edge contrast. This has a small to negligible effect on the measured resolution.

8.4. Lithographic PSF: dot-exposure method

Isolated posts were patterned with single-pixel exposures with doses ranging from 1 to 10^3fC/dot, followed by salty development[24]. The reciprocal dot dose was then plotted versus the dot radius, as described in Ref. [26], given the functional form of the point-spread function (PSF). We minimized the effect of resist development in the PSF measurement by choosing a developer (salty development[24]) with high contrast, which reduces the uncertainty of the dot-radius measurement (a detailed discussion can be found on a previous report[23]). The standard deviation for the radii of the PSF data sets (Figure 4b-c of the main text) was 0.3 nm.

9. Lithographic point-spread function and its components

The classical formulation of the lithographic PSF is a convolution of the direct-beam PSF and the SE PSF.[13, 14, 26, 27]

$$PSF_{(r)}^{litho} = PSF_{(r)}^{direct-beam} * PSF_{(r)}^{SE} \quad (13)$$

This formulation was conceived assuming that high-energy SEs are the particles responsible for delocalization of deposited energy in the resist.

Here we assumed that delocalization of deposited energy in the resist was caused by SEs, created by direct ionization of valence and core electrons ($PSF_{(r)}^{direct-SE}$), and by VPs, which may also decay into SEs. The total effect from VPs and SEs originated from VPs is $PSF_{(r)}^{VP-SE}$:

$$PSF_{(r)}^{VP-SE} = PSF_{(r)}^{VP} * PSF_{(r)}^{VP-SE\ decay} \quad (14)$$

where $PSF_{(r)}^{VP}$ is given in Figure 3d and provides the energy-density deposited by VPs. $PSF_{(r)}^{VP-SE\ decay}$ provides the energy deposition caused by SEs that originated from VPs. The $PSF_{(r)}^{VP-SE\ decay}$ may not be necessary because we have not defined whether VPs directly expose the resist or whether SEs emitted from VPs expose the resist. Either way, this $PSF_{(r)}^{VP-SE\ decay}$ has negligible spatial effect because these SEs have small energies (<50 eV), and therefore have a small maximum range (<1nm). For simplicity, we excluded the $PSF_{(r)}^{VP-SE\ decay}$

We assumed that an energy-loss event from 10 to 50 eV is due to VP excitation, and an energy-loss event from 50 to 1000 eV is due to SE generation. This division is a good approximation due to the relative cross sections of VPs and SEs in these respective energy ranges. We acknowledge that there are cascading possibilities following these primary excitations, such as excited VPs generating SEs. In addition, the excited SEs may generate VPs and other SEs. Therefore, this is a first order approximation of the effect of SEs relative to VPs. Furthermore, we note that this

approximation defines an upper limit of energy loss due to SEs and VPs because a small fraction of energy loss events at 200 keV may not directly generate a SE or VP.[8, 28]

According to the energy division above, the lithographic PSF may be written as:

$$PSF_{(r)}^{litho} \cong a \times PSF_{(r)}^{direct-beam\ E>50\ eV} * PSF_{(r)}^{direct-SE} + b \times PSF_{(r)}^{direct-beam\ E<50\ eV} * PSF_{(r)}^{VP} \quad (15)$$

According to the nomenclature in Figure 4c, we can write formula (14) as:

$$PSF_{(r)}^{litho} \cong total - energy - density_{(r)} \cong \ a \times energy - density_{(r)}^{SEs} + b \times \ energy - density_{(r)}^{VPs} \quad (16)$$

where a= 65% and b=35%, which are the percentages of measured energy loss for SEs (50<Ɛ<1000 eV) and VPs (10<Ɛ<50 eV) respectively (see Figure S3). Formula (16) was normalized by setting the spatial integration of $PSF_{(r)}^{litho}$ to unity. $energy - density_{(r)}^{SEs}$ was simulated by the Monte Carlo model described in section 7 and it was convolved with the instrument spot size. An alternative calculation would be to convolve the direct-beam PSF for energies higher than 50 eV to the SE PSF. We chose not to do this alternative calculation because the direct-beam PSF was not measured up to 1000 eV. $energy - density_{(r)}^{VPs}$ was calculated by a convolution between the direct-beam PSF for energies smaller than 50 eV and the VP PSF.

Considering that the direct-beam PSF does not change significantly between the measured range from 5 to 120 eV, we may approximate the lithographic PSF to:

$$PSF_{(r)}^{litho} \approx PSF_{(r)}^{direct-beam} * (aPSF_{(r)}^{direct-SE} + bPSF_{(r)}^{VP}) \quad (17)$$

10. References

1. Egerton, R. F. *Reports on Progress in Physics* 2009, 72, 016502.
2. Egerton, R. F., *Electron Energy-Loss Spectroscopy In The Electron Microscope*. Third Ed.; Springer New York Dordrecht Heidelberg London: 1986.
3. Silvis-Cividjian, N.; Hagen, C.; Kruit, P. *Journal of Applied Physics* 2005, 98, 084905.

4. Gonze, X.; Rignanese, G.; Verstraete, M.; Beuken, J.; Pouillon, Y.; Caracas, R.; Jollet, F.; Torrent, M.; Zerah, G.; Mikami, M.; Ghosez, P.; Veithen, M.; Raty, J.; Olevano, V.; Bruneval, F.; Reining, L.; Godby, R.; Onida, G.; Hamann, D.; Allan, D. *Zeitschrift Fur Kristallographie* 2005, 220, 558-562.
5. Ritchie, R.; Hamm, R.; Turner, J.; Wright, H.; Ashley, J.; Basbas, G. *Nuclear Tracks And Radiation Measurements* 1989, 16, 141-155.
6. Wolff, P. *Physical Review* 1953, 92, 18-23.
7. Hamm, R.; Turner, J.; Ritchie, R.; Wright, H. *Radiation Research* 1985, 104, S20-S26.
8. Udalagama, C.; Bettiol, A.; Watt, F. *Physical Review B* 2009, 80, 224107.
9. Gonze, X.; Amadon, B.; Anglade, P.; Beuken, J.; Bottin, F.; Boulanger, P.; Bruneval, F.; Caliste, D.; Caracas, R.; Cote, M.; Deutsch, T.; Genovese, L.; Ghosez, P.; Giantomassi, M.; Goedecker, S.; Hamann, D.; Hermet, P.; Jollet, F.; Jomard, G.; Leroux, S.; Mancini, M.; Mazevet, S.; Oliveira, M.; Onida, G.; Pouillon, Y.; Rangel, T.; Rignanese, G.; Sangalli, D.; Shaltaf, R.; Torrent, M.; Verstraete, M.; Zerah, G.; Zwanziger, J. *Computer Physics Communications* 2009, 180, 2582-2615.
10. Heyde, T.; Burgi, H.; Burgy, H.; Tornroos, K. *Chimia* 1991, 45, 38-40.
11. Goedecker, S.; Teter, M.; Hutter, J. *Physical Review B* 1996, 54, 1703-1710.
12. Raghunathan, A.; Hartley, J. *Journal of Vacuum Science & Technology B* 2013, 31, 011605.
13. Wu, B.; Neureuther, A. *Journal of Vacuum Science & Technology B* 2001, 19, 2508-2511.
14. Murata, K.; Kyser, D.; Ting, C. *Journal of Applied Physics* 1981, 52, 4396-4405.
15. Ghanbari, R. A. Physics And Fabrication of Quasi-One-Dimensional Conductors. Ph D, Massachusetts Institute of Technology, 1993.
16. Joy, D.; Luo, S. *Scanning* 1989, 11, 176-180.
17. Hovington, P.; Drouin, D.; Gauvin, R.; Joy, D.; Evans, N. *Scanning* 1997, 19, 29-35.
18. Drouin, D.; Hovington, P.; Gauvin, R. *Scanning* 1997, 19, 20-28.
19. Luo, S.; Joy, D. *Scanning Microscopy* 1990, 127-146.
20. Duan, H.; Manfrinato, V.; Yang, J.; Winston, D.; Cord, B.; Berggren, K. *Journal of Vacuum Science & Technology B* 2010, 28, C6H11-C6H17.
21. Duan, H.; Winston, D.; Yang, J.; Cord, B.; Manfrinato, V.; Berggren, K. *Journal of Vacuum Science & Technology B* 2010, 28, C6C58-C6C62.
22. Manfrinato, V.; Cheong, L.; Duan, H.; Winston, D.; Smith, H.; Berggren, K. *Microelectronic Engineering* 2011, 88, 3070-3074.
23. Manfrinato, V.; Zhang, L.; Su, D.; Duan, H.; Hobbs, R.; Stach, E.; Berggren, K. *Nano Letters* 2013, 13, 1555-1558.
24. Yang, J.; Berggren, K. *Journal of Vacuum Science & Technology B* 2007, 25, 2025-2029.
25. Zhu, Y.; Inada, H.; Nakamura, K.; Wall, J. *Nature Materials* 2009, 8, 808-812.
26. Rishton, S.; Kern, D. *Journal of Vacuum Science & Technology B* 1987, 5, 135-141.
27. Kyser, D.; Viswanathan, N. *Journal of Vacuum Science & Technology* 1975, 12, 1305-1308.
28. Cullen, D.; Perkins, S.; And Seltzer, S., Tables And Graphs of Electron Interaction Cross Sections From 10 Ev To 100 Gev Derived From The LLNL Evaluated Electron Data Library (EEDL), Z = 1 - 100,. Lawrence Livermore National Laboratory, UCRL-50400: 1991; Vol. 31.